ADVANCING EARTH AND SPACE SCIENCE

JGR Oceans

RESEARCH ARTICLE

10.1029/2020JC016464

Special Section:
Coastal hydrology and oceanography

Key Points:

- El Niño increases the wave power of swells generated in the extra-tropics which propagate toward the tropics
- The most significant rotations in wave direction with El Niño-Southern Oscillation (ENSO) occur at tropical and subtropical latitudes
- The global coastline was classified into five distinct types, depending on the directional wave climate response to ENSO

Supporting Information:

- Supplementary Material

Correspondence to:
I. Odériz,
itxaso.oderiz@gmail.com

Citation:
Odériz, I., Silva, R., Mortlock, T. R., & Mori, N. (2020). El niño-southern oscillation impacts on global wave climate and potential coastal hazards. *Journal of Geophysical Research: Oceans*, *125*, e2020JC016464. https://doi.org/10.1029/2020JC016464

Received 31 MAY 2020
Accepted 4 NOV 2020

El Niño-Southern Oscillation Impacts on Global Wave Climate and Potential Coastal Hazards

I. Odériz[1], R. Silva[1], T. R. Mortlock[2,3], and N. Mori[4]

[1]Institute of Engineering of National Autonomous University of Mexico, Mexico City, Mexico, [2]Risk Frontiers (RF), Sydney, Australia, [3]Department of Earth and Environmental Sciences, Macquarie University (MQ), Sydney, Australia, [4]Disaster Prevention Research Institute, Kyoto University, Kyoto, Japan

Abstract Wave direction and wave power are the main climate-related drivers of large-scale coastal morphological hazards on open sandy coastlines. El Niño-Southern Oscillation (ENSO) is the main climate driver affecting global wave climates on interannual timescales. Hence, a quantification of wave climate variability with ENSO would aid the characterization of coastal risk as a first-pass assessment tool. However, no such data are available on the global scale at present. To address this, this work (1) quantifies ENSO impacts on global mean wave direction and wave power, and (2) classifies the global coast according to the ENSO wave climate hazard. The correlation coefficient (R) of the Multivariate ENSO Index between wave power and mean wave direction was calculated. Then, employing a multivariate technique, the resulting R values were used to classify the global coastlines. The results show that ENSO has distinct latitudinal impacts around the world. El Niño increases the wave power of swells generated in the extra-tropics which propagate toward the tropics, a phenomenon which is particularly notable in the Pacific Basin, while the most significant rotations in wave direction with ENSO occur at tropical and subtropical latitudes. Based on this new information, the global coastline was classified into five distinct types, depending on the directional wave climate response to ENSO.

Plain Language Summary High ocean waves can cause erosion and flooding of coastal regions. Wave climate—the term used to describe the characteristics of ocean waves at a certain location—varies on timescales of seasons to decades. This variability can increase or reduce the amount of wave power received at the coast, affecting the probability of coastal flooding or erosion. One of the principal drivers of long-term wave climate variability is El Niño-Southern Oscillation (ENSO). This work undertakes a global analysis of wave climate response to El Niño and La Niña events along the world's coastlines. Results show that wave power is most increased/decreased during El Niño/La Niña at high latitudes (extra-tropical zone), while wave direction is most impacted at low latitudes (tropical zone). As the wave climate response to ENSO is different around the world, the global coast was classified into five types, a criterion that can be used for regional coastal planning and management.

1. Introduction

Long-term variability of the wave climate induces interannual to multidecadal fluctuations of the shoreline (Barnard et al., 2015; Kelly et al., 2019; Mortlock & Goodwin, 2016; Yates et al., 2009) as wave power and direction can be driving forces of coastal morphology. This lower frequency variability can modify erosion and flood risk on the seasonal scale (Wahl & Plant, 2015). Previous work has demonstrated the long-term wave climate variability is strongly influenced by atmospheric teleconnection, for instance: the Pacific Decadal Oscillation (Bromirski et al., 2013; Odériz et al., 2020), the Pacific/North American (Menéndez et al. 2008; Shimura et al., 2013a), or El Niño-Southern Oscillation (ENSO; Reguero et al., 2015, 2019; Semedo et al., 2010; Stopa & Cheung, 2014).

ENSO has been identified as one of the most important oscillatory mode of interannual variability of the global climate system (Neelin et al., 1998), and a primary driver of global wave climate (Stopa & Cheung, 2014). ENSO is a coupled ocean-atmosphere phenomena, which exhibits oscillatory behavior on a timescale of 2–8 years, with complex, diverse patterns (Takahashi et al., 2011). The most well-known types of ENSO are Canonical or Eastern Pacific (EP) ENSO, where the Sea Surface Temperature (SST) anomaly originates in the Eastern Pacific Ocean (Rasmusson & Carpenter, 1982) and Modoki or Central Pacific (CP)

ENSO (Ashok et al., 2007). The asymmetry, amplitude, temporal evolution, and intensity (weak, moderate, or extreme) of each ENSO event (Cai et al., 2015; Santoso et al., 2013) vary greatly. Depending on its characteristics, the effects of ENSO on the climate can be very diverse (Timmermann et al., 2018). For instance, Barnard et al. (2017) reported the extreme El Niño impacts of 2015–2016 on the West coast of the USA were different from those of previous El Niño events. Mortlock and Goodwin (2016) found that directional wave climates on the east coast of Australia showed significant differences between EP and CP ENSO types.

Previous work has demonstrated that the vulnerability of Pacific coasts is dominated by ENSO (Barnard et al., 2015; Goodwin, 2005; Ruiz de Alegría-Arzaburu & Vidal-Ruiz, 2018; Silva et al., 2017). Moreover, many studies have been carried out to identify the wave climate response to ENSO at a global scale (Mori et al., 2018; Reguero et al, 2015, 2019; Semedo et al., 2010; Stopa & Cheung, 2014). While these contributions have provided substantial information, more data is needed on ENSO coastal morphological hazards at a global scale from a physical perspective to assist in coastal management decisions, particularly for data-poor locations with limited observational networks. In particular, the mean wave directional response to ENSO, the most important driver of coastal sediment transport (Barnard et al., 2015; Morim et al., 2019; Ranasinghe, 2016; Toimil et al., 2020), still remains undocumented on a global scale.

Therefore, this work aims (1) to quantify ENSO effects on global wave direction and wave power as climate-related drivers of coastal morphological hazards, and (2) to use this information as a basis for classifying global coastal morphological hazard (based on wave direction and wave power) with ENSO. Using the latest wave reanalysis dataset, ERA 5, a global correlation approach between wave power, mean wave direction, and ENSO climate indices was developed (ONI, Oceanic Nino Index; SOI, Southern Oscillation Index; MEI, Multivariate ENSO Index; and Niño 3.4). A multivariate *k-mean* cluster was applied to identify similar ENSO responses on coasts around the world. The results showed different behaviors in each ocean basin and five coastal types were identified, with different levels of ENSO coastal morphological hazard response which we classify as Low, Moderate, High 1, High 2, and High 3. This information can be used by coastal practitioners to gain a first-pass understanding of regional-scale coastal vulnerability to ENSO which may be used to produce more detailed coastal hazard assessments at local scale. We also investigated the underlying global trends of monthly averaged wave power and wave direction over the period 1985–2018. This was done in order to contextualize the magnitude of interannual variability with the long-term trend, and to differentiate these components (i.e., variability/trend in wave power and direction) in their contribution to coastal hazards (coastal erosion and flooding) over the last four decades.

This study is organized as follows: first, the data and methods used are explained in Section 2. Section 3 describes the trends observed in wave direction and wave power. Section 4 reviews and validates ENSO climate indices. Next, the composite anomalies for ENSO phases over the past 40 years are described in order to elucidate general patterns of ENSO coastal morphological hazards. Section 5 presents the coastal classification produced in this work. Finally, a discussion of the results and conclusions are given in Sections 6 and 7.

2. Data and Methods

2.1. Wave Data

Wave power and mean wave direction are considered to be climate-related drivers of coastal morphological hazards in this work (Barnard et al., 2015; Reguero et al., 2019). In this analysis, only the deep-water wave climate is considered. Sea level or local effects, such as sea-bed interaction, or sediment supply are not considered but may also be important locally. For the calculation of these wave parameters, the latest reanalysis dataset ERA 5 (Copernicus Climate Change Service [C3S], 2017) from the European Centre for Medium-Range Weather Forecasts from 1979 to 2018 was used, with a global resolution of 0.5°. The spectral wave model used in the ERA 5 wave hindcast was HRES-WAM (Guenther et al., 1992), with 24 directions and 30 frequencies. The wave power was calculated for irregular waves, defined as $P_w = \frac{\rho g^2}{64\pi} H_s{}^2 T_e \left(W / m\right)$; where H_s (m) is the significant wave height of combined wind waves and swell, and T_e is the energy period $\left(T_e = m_{-1} / m_0 = \alpha T_{01}, s\right)$; where $\alpha = 1.08$ (Webb & Fox-Kemper, 2011) and $T_{01}(s)$ is the mean wave period. All these values were monthly averaged to allow for direct comparison with the ENSO climate indices, which are calculated monthly.

10.1029/2020JC016464

2.2. Validation of ERA 5

The ERA 5 wave dataset was validated with altimetry data GlobWave, which integrates different satellite altimeter missions (GEOSAT, ERS-1/2, TOPEX/Poseidon, GFO, Envisat, Jason-1/2, and CryoSAT), (Gavrikov et al., 2016), the spatial resolution is 1º and the temporal resolution is monthly. Given that the grid resolution of the datasets were not the same, the monthly values of ERA5 were interpolated to the grid resolution of GlobWave. For the period 1992–2013 the bias (1) was calculated for the significant wave height, on a seasonal and yearly basis:

$$Bias\left(\hat{\theta}\right) = E_{x|\theta}\left(\hat{\theta}\right) - \theta = \frac{\sum_{i=1}^{n}\left(\hat{\theta} - \theta\right)}{n} \quad (1)$$

where $\hat{\theta}$ is the estimator (ERA5) and θ is the estimated value (GlobWave). Then, the interannual validation of ERA 5 was computed. For ERA5 and GlobWave, the correlation coefficients R between ENSO climate indices (ONI, MEI, SOI, Nino3.4, as defined in detail in Section 2.4) and the significant wave height (H_s) was calculated, as explained in Section 2.5. The Bias of R between both datasets was used for interannual validation.

2.3. Long-Term Trends in Wave Power and Direction

For each time series of monthly values, the trend of P_w and Dir_m was calculated, using the Least Squares approach, where t is time and y is the variable analyzed. The method defines the total deviation of the dataset at each time step t_i, with respect to the values projected over a lineal model (Equation 1). The optimal values of the coefficients a and b are those that minimize the total deviation. Then, the yearly trend was calculated by dividing the range in the time series by the time period in years $\left(m = x_f - x_0 \ / \ t_f - t_0\right)$. The significance of the trends was calculated using the Mann-Kendall (Hirsch et al.,1982) test at a 95% level of confidence.

$$X^2 = \sum\left(y_i - \left(at_i + b\right)\right)^2 \quad (2)$$

$$Y_t = at_i + b \quad (3)$$

2.4. ENSO Climate Indices

ENSO has various impacts in space and time. For that reason, no one climate index can better represent ENSO impacts than another. Even the identification of an ENSO year was debated for several years (Ashok et al., 2007). ENSO climate indices can be classified into: those that use sea level pressure (e.g., SOI and Equatorial Southern Oscillation), the sea surface temperature indices (e.g., Niño1, Niño 1.2, Niño 3, Niño 4, and Niño 3.4), those that consider Outgoing Longwave Radiation (OLR) and finally, those that use wind or other parameters, combining more than one variable. Previous studies focusing on ocean waves used the SOI (Reguero et al., 2015), Niño 3 (Reguero et al., 2019), Niño 3.4, (Shimura et al., 2013; Stopa & Cheung, 2014), and MEI (Barnard et al., 2015, 2017). However, these authors did not establish why one or another climate index was used in their work.

In this study, four climate indices curated by the National Oceanographic and Atmospheric Administration Earth System Research Laboratory were used. Each climate index was analyzed for its statistical significance against wave power and direction, in order to identify which was the most appropriate for the description of global wave climate response to ENSO.

1. The SOI is calculated using the monthly mean Sea Level Pressure (SLP) difference between Tahiti and Darwin. During the phase of El Niño (La Niña), negative (positive) values of SOI, negative (positive) anomalies are found in Tahiti, while positive (negative) anomalies are found in Darwin
2. The Niño 3.4 is the SST anomalies of the region (5°N–5°S, 170°W–120°W) in the tropical Pacific. This index has previously been found to be the most representative for the SST regions (Trenberth & Hoar, 1997)

10.1029/2020JC016464

3. The ONI, is a 3-month moving average of the SST anomalies in the Niño 3.4 region. Values greater than 0.5 are El Niño phenomena, less than −0.5 are La Niña and values between −0.5 and 0.5 correspond to neutral phases
4. The MEI.v2 (MEI Version 2) is a bi-monthly index of the Empirical Orthogonal Function considering five variables (SLP, SST, OLR, zonal, and meridional components of the surface wind), over the tropical Pacific (30°S–30°N and 100°E–70°W)

2.5. ENSO as a Wave Climate Driver

The composite anomalies for ENSO phases (El Niño and La Niña) were computed to depict the general mechanism that affects the atmosphere and wave climate. Anomalies of individual extreme ENSO events were analyzed to detect dissimilarities that may exist between individual events. For this, the monthly anomalies (xA_{yearn}) of SLP, P_w, and Dir_m were calculated as the values of the month n of the year analyzed (x_{yearn}) minus the average of this n month for all the years ($\frac{1}{N}\sum_{i=0}^{i=N} x_{in}$).

$$xA_{year\,n} = x_{year\,n} - \frac{1}{N}\sum_{i=0}^{i=N} x_{in}; n = 1,2,\ldots,12 \tag{4}$$

The general effects of ENSO on mean wave direction and wave power were calculated using the correlation coefficient between the residual time series of P_w and Dir_m and the MEI, ONI, SOI, and Niño 3.4 climate indices. The time series were considered as an Additive Model ($X_t = T_t + S_t + R_t$.), then the residuals R_t were calculated, removing the trend (T_t) and the seasonal component (S_t). The seasonal component (S_t) was calculated by applying a moving average for the 12 months.

The correlation coefficients were calculated using the Pearson approach (Kendall, 1948) with a level of confidence of 95%. When the probability was less than 5% ($p < 0.05$) the correlation coefficient was considered as statistically significant. From Equation 4, $\overline{x_A}$ and s_A are the mean and standard deviations of the variable A (Climate Index) and $\overline{x_B}$ and s_B of the variable B (wave power and mean wave direction). Cross correlation was computed within a 12-month lag window to find the lag when the maximum value of R was obtained. Only values statistically significant were considered for the analysis. A 12-month window was used based on a typical duration time of an ENSO event. This time is dependent on the travel time of oceanic Rossby waves to reach the land boundaries and for subsequent reflection of Kelvin waves that dissipate the ENSO signal. The results of months are presented in absolute values.

$$R(A,B) = \frac{1}{N-1}\sum_{i=1}^{N}\overline{\left(\frac{A_i - \overline{x_A}}{s_A}\right)}\left(\frac{B_i - \overline{x_B}}{s_B}\right) \tag{5}$$

2.6. Coastal Classification

The second aim of this work was to identify the patterns of ENSO coastal hazards around the world. A multivariate *k-mean* clustering technique (MacQueen, 1967) was used to detect spatial patterns of ENSO impacts on wave climate, applying the MATLAB® Statistics and Machine Learning Toolbox. This technique gathers variables with similar characteristics, creating clusters based on the similarity (near) and dissimilarity (far) of the variables of other clusters. The method uses the Euclidian distance from a point x_i, to the centroid C_i (Equation 5). The classification variables were the R_{lag0} (MEI-P_W) and $R_{\ lag0}$ (MEI-Dir_m) for coasts worldwide. These variables were normalized, from 0 to 1, to give the same weight to each variable in the Euclidian distance. The optimal number was calculated by repeating the *k-mean* clustering technique from 2 to 10 clusters. For each number of clusters, the sum of the squared error (SSE) of the distance and the Silhouette coefficient (Kaufman & Rousseeuw, 1990) were calculated. Then, the SSE versus the number of clusters were plotted and the Elbow Method was applied. The Silhouette criterion was applied by selecting the maximum value of all the Silhouette coefficients obtained.

$$d(x,C) = \sqrt{\sum_{i=1}^{n}(x_i, C_i)^2} \tag{6}$$

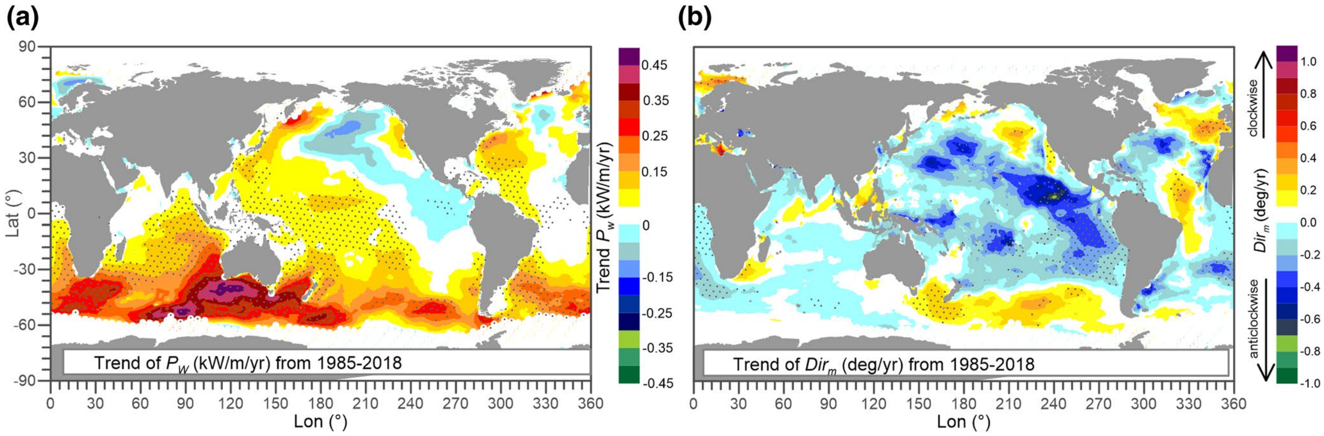

Figure 1. (a) Global annual trend of P_w from 1985 to 2018; (b) global trend of Dir_m from 1985 to 2018. The dots mark the trends that are significant, at 95% confidence level.

3. Global Trends

First, we investigated the global trends (1985–2018) of monthly averaged wave power and mean wave direction, to differentiate them from interannual variability, and in order to later compare them in detail as climate drivers of long-term coastal morphological hazards. The initial year of the time range was selected, as the year when the first altimeter wave data, GEOSAT, was available (Young et al., 2011). The global trends for the period 1979–2018 was also calculated, with no large differences (Figure S9 in Supporting Information). Figure 1a shows that wave power tends to increase in all the ocean basins, with the exceptions of the northcentral and tropical east Pacific. The trends in P_w show a latitudinal variation, with the highest values found in the Southern Ocean, with an increase from 0.2 to 0.4 kW/m/year, and the lowest values found in the tropical belts, from 0.02 to 0.15 kW/m/year. These effects had been already demonstrated in global winds (Ribal & Young, 2019), and in wave climate (Babanin et al., 2019; Ribal & Young, 2019; Young et al., 2011). The trends 1985–2018 resemble the robust consensus that an increment of the mean and high percentiles of H_s in the Southern Ocean exists (Ribal & Young, 2019; Young et al., 2011). The power of the waves propagating from the Southern Ocean, from where most of the swell waves radiate across the Pacific, Indian, and South Atlantic Oceans (Alves, 2006; Babanin et al., 2019), could be the reason for the increase in wave power in almost all the ocean basins (Morim et al., 2019). This agrees with the changes found in atmospheric circulation, where the Hadley Cell expands poleward, leading to reduced intensity in the tropical circulation. This expansion also magnifies the extratropical westerly winds in the positive phase of the annular modes, which is particularly clear in the southern hemisphere (Reichler, 2009). On the other hand, the Aleutian Low is projected to decrease (Lu et al., 2008), which could explain the reduction in wave power in the North Pacific 1985–2018. The spatial patterns and magnitude obtained for wave power trends from 1985 to 2008 (Figure S12 in Supporting Information) are broadly similar on the global scale to those obtained by Reguero et al. (2019). However, some dissimilarities exist between this analysis and that of Reguero et al. (2019) for the Pacific coasts of South America. This region is affected by energetic swells generated in the Southern Ocean and the main source of difference might be related to the reanalysis used (GOW vs. ERA 5). GOW was forced by WaveWatch III (Tolman, 2009), and ERA 5 by WAM (Guenther et al., 1992). While we do not purport to know which approach is best, we note that the relatively new ERA 5 wave hindcast performs consistently well for significant wave height when compared with global altimetry observations (Timmermans et al., 2020) and with the seasonal and long-term variability of GlobWave as shown in Figures S1, S2, and 2.

From the trends analysis, the mean wave direction shifts anticlockwise (blue) in almost all of the ocean basins, while in the extratropical and tropical Indian Ocean, and tropical South Atlantic, the wave direction shifts clockwise. Significant clockwise shifts in wave direction are found in the South Pacific and the Northeast Atlantic (0.3 degrees/year, or approximately 10 degrees over the period 1985–2018), while a significant anticlockwise rotation is found in the Tropical East Pacific (up to 0.7 degrees/year, or approximately 24

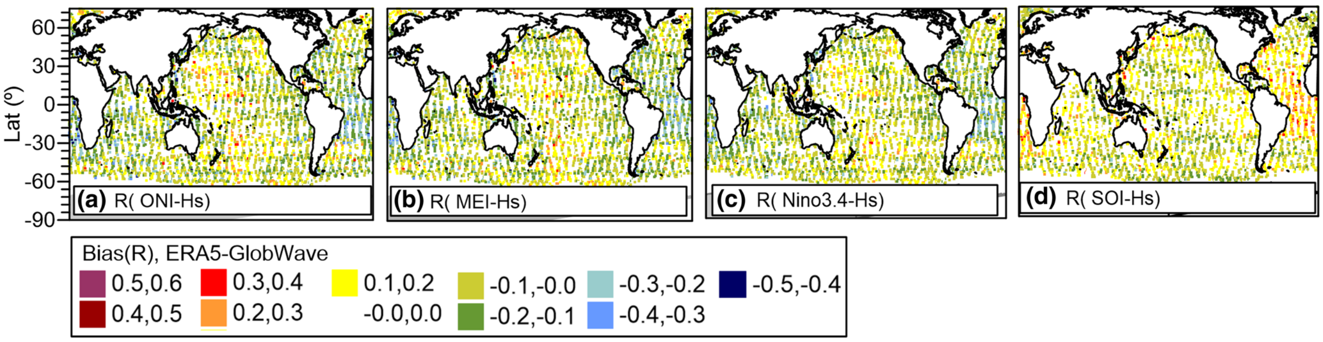

Figure 2. Bias of Correlation Coefficients (calculated sequentially between ENSO climate indices and ERA-5 derived H_s, and same again for GlobWave H_s) from 1992 to 2013. (a) ONI, (b) MEI, (c) Nino 3.4, and (d) SOI. ENSO, El Niño-Southern Oscillation; MEI, Multivariate ENSO Index; ONI, Oceanic Nino Index; SOI, Southern Oscillation Index.

degrees for the analysis period). Since the prevailing wave direction in the South Tasman Sea (Australia/New Zealand) is southeasterly, and is northeasterly in the Northeast Pacific (Mexican Pacific and Californian coast), these changes signify a rotation toward the south in both locations.

4. ENSO as a Wave Climate Driver

In this section the interannual variability in the general pattern of the directional wave climate induced by ENSO, is analyzed. The potential differences that may exist between individual events is also highlighted. Prior to this analysis, we present a validation of the seasonal and interannual variability in ERA5 wave heights against global altimetry measurements.

4.1. Validation of ERA5 Seasonal to Interannual Variability

In general, significant wave heights from ERA 5 are negatively biased for seasonal variability when compared to the altimetry dataset Globwave (see Figure S1), suggesting the amplitude of seasonal variation in wave height is underestimated. Occasionally, positive bias values were found on the western boundaries of the Atlantic and Pacific basins, in areas generally having a larger fetch and receiving longer-period swells from the Southern Ocean. The Asian Monsoon region also presented a positive bias. This overestimation increases in autumn and decreases in spring.

ERA 5 showed a generally good performance in replicating interannual variability compared to altimetry measurements, much improved on the seasonal validation, with similar spatial patterns of R as the Globwave dataset (see the R-maps in Figure S2 and the R-bias in Figure 2). As it can be seen, results show low values of bias (±0.2).

4.2. ENSO Climate Indices

As explained previously, there is no specific climate index that is best to analyze ENSO impacts. It depends on the region and the variable studied. In this section, we analyze which ENSO index is best for an analysis of global wave power and direction. For this, the statistical significance of correlation coefficients (Figure 3) between P_w and Dir_m and each climate index, and their difference in magnitude (Figure S16) were calculated for all the ocean basins. Although both values were compared, we used statistical significance as the robustness criteria to identify correlation. The climate index with the most statistically significant points will be that which covers the ENSO phenomenon spatially best over the global scale. Some areas may show high magnitude difference in R values, but if these occur in areas where the relationship between wave parameters and the ENSO index is not statistically significant, the magnitude difference may not be a good descriptor of the robustness of the ENSO index. Nevertheless, the differences in magnitudes between R values are also analyzed on a regional basis.

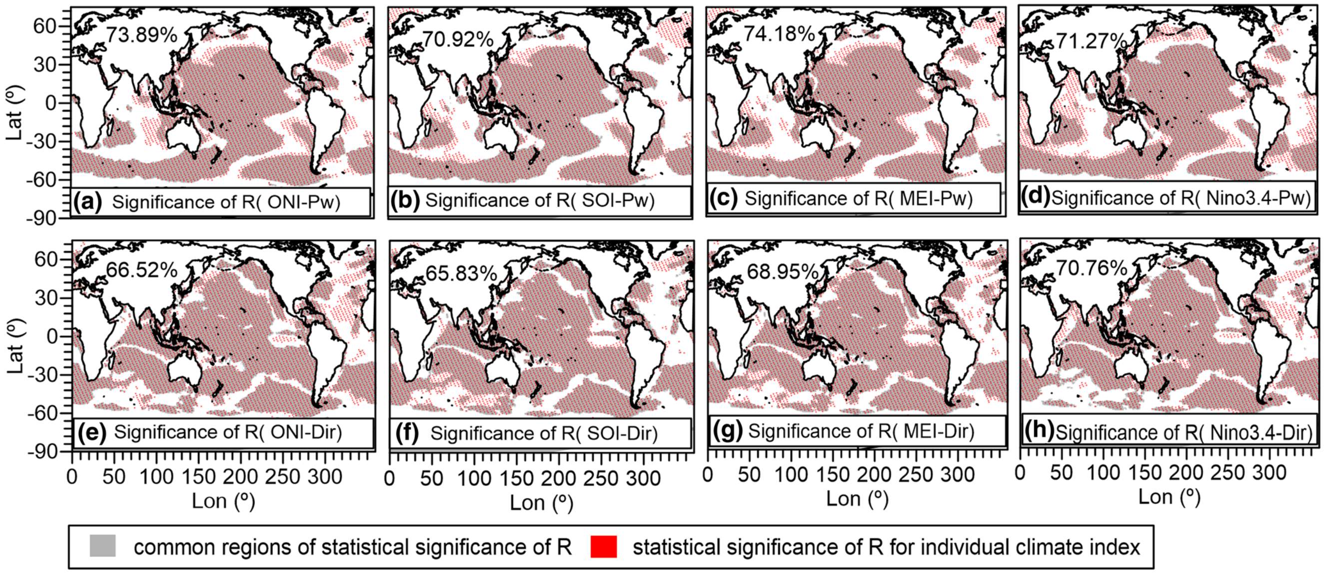

Figure 3. Statistical significance of the ENSO Climate Index for wave power and mean wave direction. The top and bottom panels are P_w (a, b, c, d) and Dir_m(e,f, g, h), respectively. The first column shows the SOI (a, e), the second the ONI (b, f), the third the Nino 3.4 (c, g), and the fourth the MEI (d, h). The red dots mark significant correlation points and the values are the percentage of statistically significant spatial cells worldwide. ENSO, El Niño-Southern Oscillation; MEI, Multivariate ENSO Index; ONI, Oceanic Nino Index; SOI, Southern Oscillation Index.

Each climate index considers different regions and parameters. For example, the SOI, which has the poorest results for global analysis, uses the SLP for part of the southern hemisphere. Meanwhile, the ONI, MEI, and Niño 3.4, which give better results, are calculated for regions in the tropical Pacific, where the phenomenon is produced. Although, the ONI and Niño 3.4 use the same SST database, the former uses a moving average of the anomalies of SST for 3 months, and the second uses the monthly average. The differences in the percentages presented for the P_w and Dir_m for each climate index might be associated with the fact that the ENSO impact in the P_w is delayed (it might take more than 1 month to see ENSO impacts in the P_w), while the Dir_m response to ENSO is evident in a shorter period of time. For example, the values obtained for the climate index Niño 3.4 is used with the SST of the tropical Pacific of each month, which is highly correlated with the wave direction, (Figure 3h). However, correlation between wave power and Niño 3.4 is the second-worst performer of all indices. Instead, ONI or MEI—both which use a moving average of 2 and 3 months, respectively—perform better (Figures 3e and 3g). This suggests that the wave power response to ENSO may be lagged in accordance with timescales used by the MEI and ONI.

The spatial distribution of the statistical significance of R shows, as expected, that the Pacific is the ocean basin with greatest area of response to ENSO, followed by the Indian Ocean and then the Atlantic. As Figure 3 illustrates, the spatial response to ENSO is different for the two variables. P_w responds more to ENSO than Dir_m globally. The Indian Ocean, in particular, is more affected by ENSO in the mean wave direction. The opposite occurs in the Southern Ocean, where wave power is significantly correlated across the whole belt, but not wave direction. The common regions for all the ENSO climate indices, where the R are statistical significance are those where the individual ENSO events impact similarly always (Figure 3). However, those regions where the statistical significance is not consistent for all the climate indices are transitions frontiers where the individual ENSO events impact are different each time. The difference in magnitude between the ENSO climate indices (Figure S16) shows MEI reaches higher values globally distributed. However, Niño 3.4 shows especially higher values of R in the Monsoon area, while the wave power is clearly biased by hemisphere, with higher correlation values in the Southern Hemisphere. The values of the SOI index were the highest in the East Indian Ocean.

It can be said that globally no large differences, were found between the climate indices analyzed, in magnitude nor in spatial patterns. For P_w, the climate index offering the highest significance is the MEI and, for direction, the Niño 3.4, followed by the MEI. The climate index selected for this work was the MEI, because this index gives the best results for P_w, and the second best for Dir_m (from a global perspective).

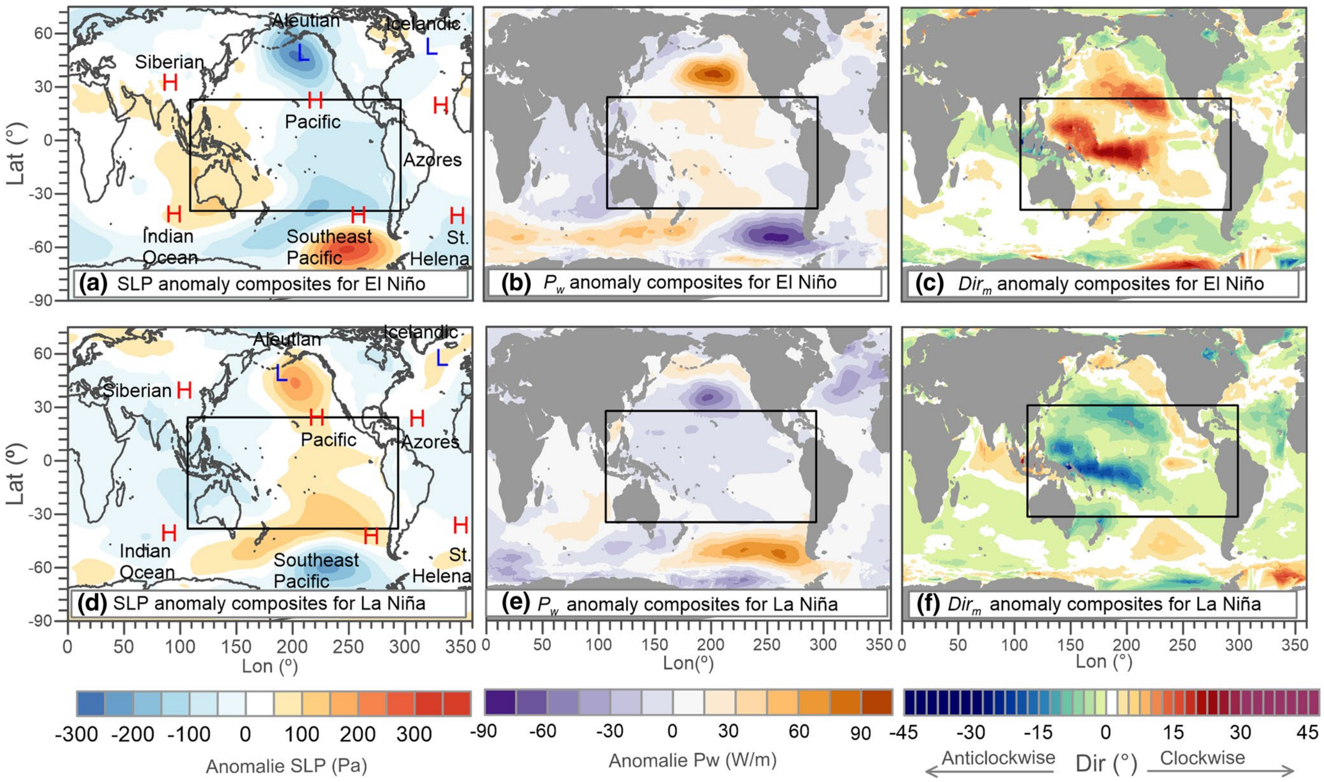

Figure 4. SLP (a and d), P_w (b and e) and Dir_m (c and f) composite anomalies for warm and cold phases of ENSO. Top panels (a–c), correspond to El Niño and bottom panels to La Niña. H and L in the SLP panels indicate high- and low-pressure systems. SLP, Sea Level Pressure.

4.3. Composite Anomalies for ENSO Phases

In this section we provide the basis for the correlation analysis by investigating the composite anomalies of atmospheric and ocean configurations in ENSO phases. Figure 4 describes the anomalies in SLP (Figures 4a and 4d), P_w (Figures 4b and 4e) and Dir_m (Figures 4c and 4f) for El Niño and La Niña. In the Supporting Information (Figure S14) the anomalies are depicted for three extreme ENSO events: El Niño 1997–1998, La Niña 2010–2011, and El Niño 2015–2016. Those events were selected as they have the higher values in ONI. The composite anomalies 1979–2018 show a general pattern, but the individual events here analyzed show also dissimilarities between them.

The ENSO phenomenon originates in the tropical Pacific, as shown by the rectangle marked in Figure 4 panels. During canonical El Niño events, this region shows positive anomalies in SLP in the west and negative anomalies in the east Pacific. This produces a weakening of the easterly equatorial trade winds, or even a reverse in their direction (Reiter, 1978), in contrast to the strengthening of wave power in the tropical Pacific (see Figure 4b).

During El Niño, in the North Pacific, the winds shift clockwise, due to the positive anomalies of SLP over the northern subtropical Pacific (Wallace & Gutzler, 1981; H. Wang et al., 2012). However, El Niño events produce an anomalously deep Aleutian Low (Figure 4a) and the wind strengthens anticlockwise in the Northwest Pacific coast. This increases the wave power (Figure 4b) and the mean wave direction shifts northward (Figure 4c). However, during the 2015–2016 event the wave fields rotated toward the south, due to a different distribution in SLP during this event (Figures S14a and S14b). This dissimilarity in the wave direction during the 2015–2016 El Niño was reported by (Barnard et al., 2017). During El Niño, in the South Pacific, a mirror effect is produced in the SLP, where two blocking high pressure systems become quasistationary in this area (Fogt & Bromwich, 2006). This leads to a reduction in wave power and a rotation of the wavefield northward around the Magellan Straits. In the rest of the Southern Ocean, the wave power increases during El Niño. During the 2015–2016 event, the North Pacific experienced a larger increase in

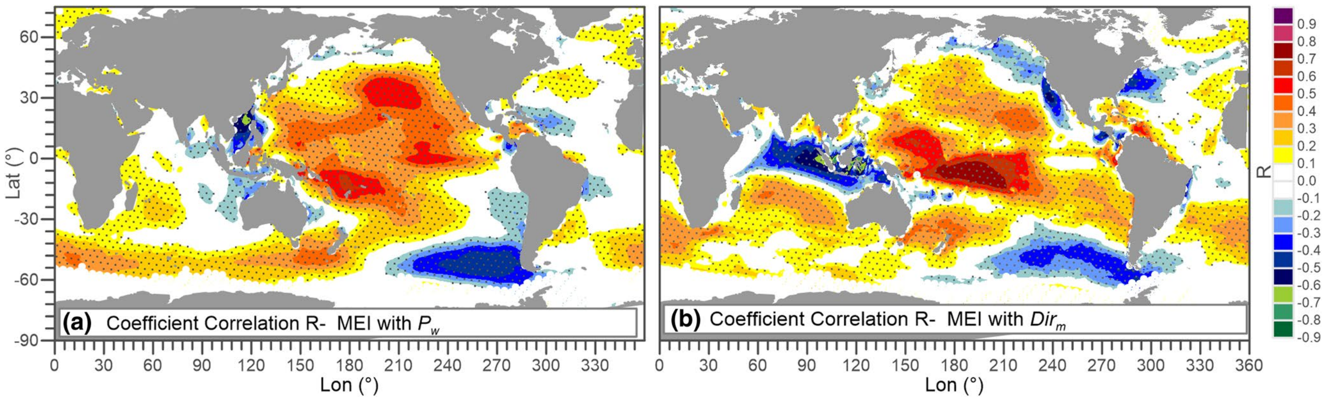

Figure 5. Correlation coefficients of MEI and; (a) wave power; (b) mean wave direction. The black dots mark significant correlation points at a significance level of 95%. MEI, Multivariate ENSO Index.

wave power, while the South Pacific showed larger positive anomalies in P_w during the 1997–1998 event. This could point to a pronounced hemispheric asymmetry of ENSO which other authors have also noted (e.g., Timmermann et al., 2018). In the Indian Ocean, wave power generally weakens during El Niño, as a result of the strong positive anomalies that occur over the Philippine Sea (East Pacific). During El Niño in the North Atlantic, the Icelandic Low normally intensifies (Moron & Gouirand, 2003), which increases wave power and rotates the wavefield clockwise. The El Niño extreme event impacts in 1997–1998 and 2015–2016, however, were not identical for the North Atlantic margins including the coasts of Europe, USA, and Gulf of Mexico, as shown in (Figures S14d, S14e, S14g, and S14h).

During La Niña, global teleconnected SLP anomalies are inverted with respect to EL Niño events (B. Wang et al., 2000), (Figure 4d), producing a general decrease in wave power, with the exception of the East Indian Ocean, the Northwest Pacific, the Northwest Atlantic, and part of the Southern Ocean. The wave fields turn clockwise in the Northeast Indian Ocean during ENSO cold phases. In general, the spatial patterns of La Niña events tend to be weaker than El Niño and are more similar between each other (Timmermann et al., 2018).

4.4. ENSO as a Driver of Wave Climate: General Patterns

The previous analysis demonstrates that, while there are similarities in the basin-wide wave climate response during ENSO events, there remains some considerable variability between events. In an effort to find generalized behavior, the Correlation Coefficients between the MEI and the residuals time series of P_w and Dir_m were calculated for the 1979 to 2018 period (Figure 5). During warm phases of ENSO, Figure 5 shows that wave power in the Southern Ocean intensifies and the waves are more northerly with the exception of the Southeast Pacific, where this power lessens, due to the blocking pressure in the Southeast Pacific, as mentioned earlier.

The wave power responses were similar in the central Pacific (R~0.4), where the trade winds are weaker than in ENSO neutral phase. However, the Hadley Cell contracts and strengthens and the branches intensify westerly and shift poleward, leading to a strengthening of the subtropical Jet stream in both hemispheres (Lu et al., 2008; Reichler, 2009). Thus, the swell radiated from the extratropical belts to the tropical belt is intensified.

In the monsoon region during the warm phase of ENSO wave energy reduces, as has also been reported by (B. Wang et al., 2000; Zhang et al., 2016), who noted that El Niño creates weaker monsoon winds, which shift clockwise.

In general, in ENSO events the mean wave direction follows a well-defined regional deviation. It is positively correlated in the north and in the subtropics of the Indian Ocean, (R~0.3), southern subtropics of all the basins, and tropics of the Pacific (R from 0.3 to 0.7) and the Atlantic (R~0.2). Concurrently, in the tropical Indian Ocean, tropical Pacific, and North Atlantic, R acquires negative values in the North Pacific (central

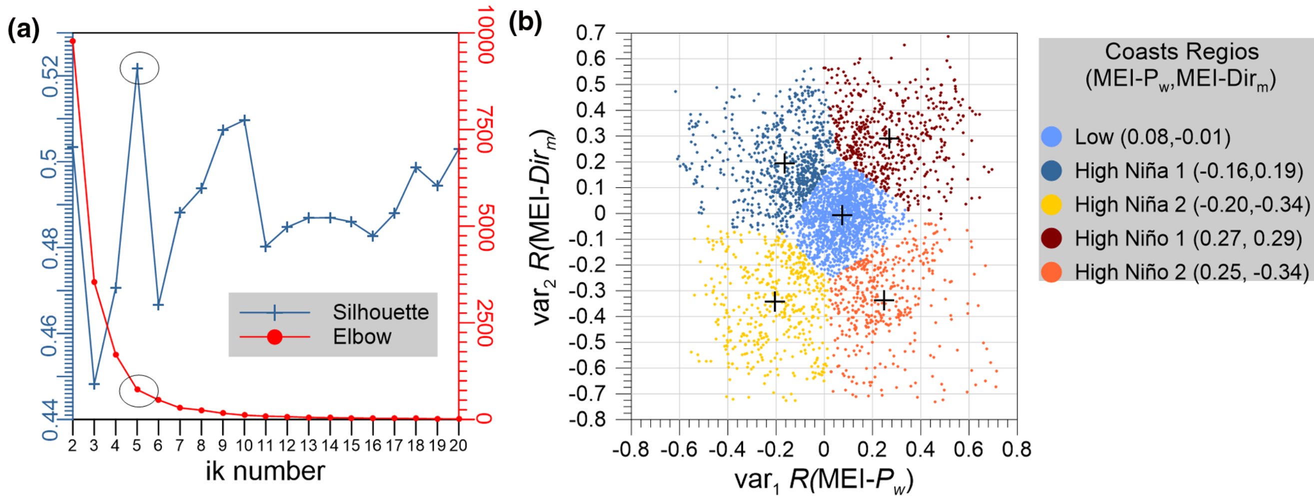

Figure 6. (a) Elbow and Silhouette criteria to identify the optimal number of clusters; (b) the cluster classification for both variables.

and east), (R~−0.3), and northern extratropics of the Atlantic (R~−0.25). The extratropics and subtropics were positively correlated (R~0.15) in the Atlantic. This is a response to the poleward movement of the subtropical jets during El Niño (Reichler, 2009). Stronger correlations were seen in the Caribbean Sea (R~0.4).

The lagged cross-correlation analysis showed that the effects of ENSO vary temporally on a basin-by-basin basis. Effects are almost immediate (highest R values within 0–3 months) for wave power in the Pacific basin and the Southern Ocean region of Australia. By comparison, the wave power response in the Atlantic is lagged by up to 12 months with respect the original ENSO climate signal. The mean wave direction responded earlier than wave power, as was hypothesized when the climate indices were compared. Figure S17 shows the maximum values of R within a given 12 month period. In general, it can be seen that the extratropics of all ocean basins are the most influenced by the ENSO signal in terms of wave power, while a wave directional response is most significant in the Northern Hadley Cell and Subtropical Ridge regions of the North Pacific.

From the findings, general patterns of ENSO can be seen that force a latitudinal response in the wave climate due to the anomalies identified in the atmospheric circulation. However, not all ENSO events produce the same anomalies in SLP, or in P_w and Dir_m, and the coastal hazards can be expected to vary on an event-by-event basis, depending on the ENSO characteristics, such as was the case for the 1997–1998 and 2015–2016 El Niño events.

5. ENSO Coastal Hazard Patterns

For classifying the global coast according to vulnerability to interannual ENSO wave impacts, the correlation and pattern analysis undertaken above were used. In order to identify coastal patterns, the *R-lag 0* results were extracted for global coastlines, see Figure S11 in Supporting Information. Overall, R_{lag0} (P_w and Dir_m) values were found to be most significant in the Americas, Southeast Asia, and Oceania, whereas Africa and Europe show minimal correlation.

Although the R-maps in the Supporting Information section are useful as input data for the global coastal community, for management criteria a coastal classification is more practical for creating an index that identifies coasts with similar ENSO impacts on interannual wave climate variability. The classification presented here was carried out by clustering the R of MEI-P_w and MEI-Dir_m, using the *K-mean* cluster technique for all the world's coasts, (see Data and Methods for detail). Using the Elbow and Silhouette criteria, the optimal number of clusters was found to be 5, (Figure 6a). In Figure 6b, the variables used ($R_{MEI\text{-}Pw}$ vs. $R_{MEI\text{-}Dirm}$) in the cluster are presented, and the five groups are shown to be reasonably well defined in two-dimensional space.

10.1029/2020JC016464

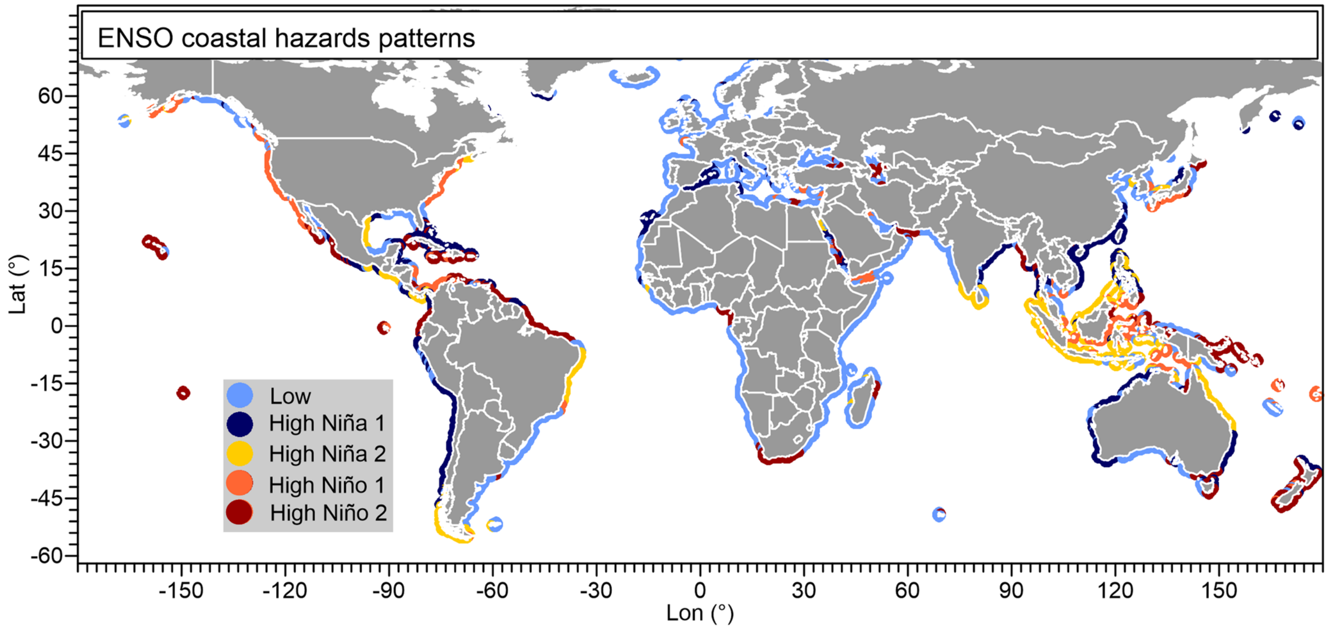

Figure 7. Coastal classification as a function of the level of directional wave power variability with ENSO. ENSO, El Niño-Southern Oscillation.

Figure 7 shows this coastal classification projected on a world map. The description of each level is as follows:

1. Coasts with a low response to ENSO events (light blue): These coasts (e.g., Argentina Uruguay, Iceland, Portugal, Mauritania, Angola, and Iran) respond to El Niño and La Niña but within a range of ±0.2 for R (P_w and Dir_m)
2. Coasts of High Niña 1 ENSO response (dark blue): These areas exhibit a reduction (increase) in wave power and a clockwise (anticlockwise) rotation of the wavefield during El Niño (La Niña). The coastal response is from 0 to 0.6 for R-Dir_m and from −0.6 to 0 for R-P_w. In all cases one or both of the R-Dir_m and R-P_w values are greater than 0.2. The coasts of Southeast Australia, North of North Island New Zealand, Southeast China, East India, and East Cuba are all included in this classification band
3. Coasts of High Niña 2 ENSO response (yellow): In these areas wave power reduces (increases) but turns anticlockwise (clockwise) during El Niño (La Niña) events. Both Dir_m and P_w are negative, and at least one is less than −0.2, with the R correlation ranging from −0.6 to 0. E.g., Indonesia
4. Coasts of High Niño 1 ENSO response (orange): wave power increases (reduces) and turns anticlockwise (clockwise) during El Niño (La Niña) events. For P_w 0 to 0.5 and for Dir_m. −0.5 to 0, with one of the variables always exceeding ±0.2 of R. In this classification are the coasts of the US and South Japan
5. Coasts of High Niño 2 ENSO response (maroon): In these areas wave power increases (reduces) and turns clockwise (anticlockwise) during El Niño (La Niña) events. In this classification both P_w and Dir_m are positively correlated and the greatest values of R are found. Coasts in this classification include: most of New Zealand, South Africa, West Cuba, West Mexico, and Hawaii

The results plotted in Figure 7 show the level of coastal response (wave power and direction) to ENSO events, which ultimately have implications for a wide range of applications, stretching from sediment budgets, erosion/accretion cycles, the harvesting of wave energy to coastal ecosystem conservation.

This information is useful not only for demonstrating coastal ENSO connectivity on a global scale, but also more practically for coastal managers to better anticipate interannual coastline response to ENSO at regional level. For example, wave power may be expected to increase during La Niña events in High Niña 1 and 2 classification bands, but only during El Niño events for High Niño 1 and 2 regions. Similarly, a clockwise shift in wave direction can be expected for High Niña 2 and 1 regions during La Niña, whereas this reverse rotation occurs during El Niño events for High Niña 1 and 2 locations also.

6. Discussion

The investigation of the effects induced by ENSO has become of key interest in medium and long term coastal management (Barnard et al., 2015, 2017; Escudero et al., 2019; Medellín & Torres-Freyermuth, 2019; Mortlock & Goodwin, 2016; Ruizde Alegría-Arzaburu & Vidal-Ruiz, 2018; Storlazzi & Griggs, 1998; Storlazzi & Reid, 2010) due to its impact on coastal risk, wave power extraction and coastal ecosystem responses. The results presented here give an insight into global patterns of interannual variability of wave direction and wave power driven by ENSO, as one of the primary climate-related drivers of basin-wide coastal vulnerability (Barnard et al., 2015; Morim et al., 2019).

6.1. ENSO as a Wave Climate Driver

In the analysis of global direction and wave power, no consensus had been established as to which ENSO climate index should be used. The present study found that the MEI is the best climate index to study global wave power, and the Niño 3.4 index is the best to analyze global mean wave direction. In this study, the MEI was selected as the most appropriate climate index to analyze wave direction and wave power at the global scale.

The results show a general global ENSO wave climate pattern, which varies according to latitude. In particular, during El Niño, wave power increases in the extratropics of both hemispheres for the three ocean basins, in response to the strength of the westerly winds in the extratropical Pacific, Atlantic and Indian Oceans (Timmermann et al., 2018). In the tropics there is also an intensification of wave power, caused by the swell propagated from the extratropics. This is consistent with the strengthening of the subtropical jets in both hemispheres during El Niño (Lu et al., 2008; Reichler, 2009). Regions of special interest, such as the Indian Monsoon and the Tropical Warm Pool, show a decrease in wave power during ENSO warm phases. The latitudinal variation in wave direction is even clearer; in the southern subtropics this turns clockwise, coming from the north, while in the extratropics, particularly in the northern hemisphere, it shifts anticlockwise, coming southerly direction. This is because the Aleutian Low strengthens and is displaced northeast, producing more southerly winds at the land-sea boundary of North America. This is in agreement with the observations found by Lu et al. (2008) and Reichler (2009), that the subtropical jets move poleward during El Niño events. The most direct impacts of ENSO were found in the Pacific Ocean, followed by the Indian Ocean, which has a similar delay in the wave direction but more delays in wave power, while the effects delay 7–12 months to impact ocean Atlantic.

We conclude that the atmospheric teleconnection induced by ENSO in the extratropics produces the greatest impact in wave power, and the response in mean wave direction is most notable in the tropics and subtropics. These findings are consistent with the theoretical results of ENSO mechanism variability and are in agreement with the results of other authors (Reguero et al., 2019; Semedo et al., 2010; Shimura et al., 2013; Stopa & Cheung, 2014). While there are general patterns of wave direction and wave power produced during ENSO events, the anomalies also highlight dissimilarities in the direction and wave power in different events, as noted by Barnard et al. (2017). These anomalies are likely to be relevant for event-specific patterns in long-shore and cross-shore sediment transport. The estimation of ENSO impacts on wave climate needs more investigation, particularly in identifying the impacts associated to the particular ENSO characteristics, such as intensity, temporal evolution, or asymmetry. For example, the asymmetry of ENSO is related to the intensification of extratropical westerly winds during El Niño events (Timmermann et al., 2018). A more accurate prediction of the wave climate impacts under different ENSO characteristics may lead to a reduction in the uncertainties of ENSO-driven sediment transport.

6.2. ENSO Coastal Hazards and Climate Change

Both climate change and atmospheric climate variability affect wave climate from the event to multidecadal scale, and must be considered for sustainable coastal management practice (Toimil et al., 2020). While global warming has been reported by the IPCC Fourth Assessment Report to resemble an El Niño–like SST pattern in the Pacific, the meridional response of the atmosphere does not conform to this (Lu et al., 2008).

In the warm phases of ENSO, the Hadley Cells contract and intensify, the extratropical westerly zonal winds shift equatorward, the Aleutian low strengthens and the subtropical highs move toward the equator, which is the opposite to what happens with global warming. However, both of them weaken the Walker Circulation (Lu et al., 2009; Lucas et al., 2014; Reichler, 2009). From this, some responses in global warming and in ENSO warm phases are similar, particularly the increase in wave power in the Southern Ocean, where the swells are irradiated toward the ocean basins (Babanin et al., 2019) following the patterns identified by Alves (2006). In the areas affected by these swells, such as Australia, Africa, or America, the phenomena, when coupled, can expose these coasts to high levels of risk.

In the northern hemisphere, in the center-east Pacific, wave power is expected to decrease, therefore the ENSO effects could be reduced in these regions. However, ENSO effects may amplify directional changes in the extratopics of the Pacific, North Atlantic, southern Indian Ocean, and on the Atlantic coast of South America. In the Southeast Atlantic and Pacific these shifts, produced by ENSO events, could be dampened by global warming. In general, the mean wave direction shifts anticlockwise in the tropical and subtropical Pacific, and in the subtropical Atlantic. In the extratropics, the waves tend to turn further clockwise. The coupling of the global warming trend with ENSO can significantly dampen or amplify wave power impacts.

6.3. Integration of ENSO Response in Coastal Assessment

The regions with highest ENSO response are identified as the Pacific, Northwest Atlantic, and the eastern Indian Ocean, while lower responses are found for African and European coasts. This classification at global level is in accordance with results published for particular cases, for instance those identified by Barnard et al. (2015). The classification can be used to identify regions with most risk to ENSO effects, allowing coastal decision makers to prioritize the regions where adaptation strategies are most needed. This is most valuable in areas where observations are limited or provide insufficient information. It should be said that this study focuses only on incoming waves as climate-related drivers of coastal hazards, while other factors can modify these effects, such as sea level rise, storm surges, tides, extreme fluvial discharges, and local effects, (sediment supplies, sea bed interactions, or coastal infrastructure projects). All these factors should be considered in holistic assessments of coastal risk (Goodwin et al., 2016; Storlazzi & Reid, 2010; Toimil et al., 2020).

This study has focused on monthly average wave conditions and the native resolution of the reanalysis used was 0.5°. As such, our analysis does not focus on storm wave conditions, but rather the bulk (i.e., modal plus storm) wave climate as the principle driver of the long-term (i.e., seasonal to multidecadal) sediment budget. While episodic erosion and flooding events associated with extreme ENSO wave conditions are often the focus of such studies, the longer-term fluctuations (seasonal and greater) in directional wave power is another important component of coastal risk as it preconditions coastal systems for extreme events. In addition, an increase (decrease) in monthly mean bulk wave power is likely an indication of increased (decreased) storminess over a seasonal basis, at least. While the influence of extra-tropical storms will be captured in the hindcast wave data and in our analysis, tropical cyclones are likely to be underestimated as reanalysis winds used to drive the wave hindcast are not of sufficient resolution to properly capture tropical cyclone intensities. This problem is common to all reanalysis-driven wave hindcasts. A subsequent study to this with a specific focus on extreme ENSO wave events is in progress.

7. Conclusions

In this work two key climate-related drivers of coastal morphological hazards, P_W and Dir_m, are analyzed in relation to their interannual variability forced by ENSO. First, a global statistical analysis was carried out, showing that the most accurate ENSO climate index for Dir_m, is the Niño 3.4 index, and for P_w, the MEI index. These results establish a framework for a better selection of ENSO climate indices for regional and local coastal and wave climate studies.

Importantly, this work has identified a strong latitudinal stratification of global ENSO wave climate, and shows that ENSO impacts wave power most in the extratropics, while wave direction is affected most in the tropics and subtropics. This reinforces the notion of ENSO as a global coastal phenomenon, with a direct physical connection in the Pacific Basin and more indirect effects in other areas via atmospheric teleconnections and trans-basin swell propagation. Both global warming and ENSO warm phases intensify the swell produced in the Southern Ocean, and the combination of these two phenomena can amplify the coastal risks along coastlines affected by them.

A classification of the world's coasts was presented, based on interannual directional wave climate variability with ENSO, which is viewed as a major climate driver of coastal vulnerability. Coasts with a Low ENSO response are little affected, while for those of High Niña 1 response the wave power decreases (increases) and turns clockwise (anticlockwise) during El Niño (La Niña) to a small degree. For coasts where the impact of ENSO is High Niña 2, the wave power decreases (increases) and turns anticlockwise (clockwise) during El Niño (La Niña). Where the response to ENSO is classified as High Niño 1 the wave power increases (reduces) and turns anticlockwise (clockwise) during El Niño (La Niña). High Niño 2 response refers to areas where the wave power increases (decreases) and turns clockwise (anticlockwise) during El Niño (La Niña).

This coastal classification offers a criterion for the identification of long term patterns of ENSO-related coastal hazards, which can be used by coastal communities to develop adaptation plans, extract wave energy, or manage port operations.

Although the results obtained here offer a robust base of knowledge for the management of coastal morphological hazards driven by ENSO, more work is needed to describe the interaction between ENSO and ocean waves. This is particularly the case for the quantification of impacts on the wave climate for individual ENSO events with different characteristics (asymmetry, amplitude, temporal evolution and intensity). Understanding the stages or intensity of ENSO events would greatly aid our comprehension of the underlying mechanisms and lead to more reliable projections of coastal risk around the world.

Data Availability Statement

The authors would also like to acknowledge the provision of open data sources by the US National Oceanographic and Atmospheric Administration Earth System Research Laboratory (https://www.esrl.noaa.gov/psd/data/climateindices/list/) and the European Centre for Medium-Range Weather Forecasts. The repository data of this work is provided in https://doi.org/10.17632/t8rrbn9ynd.1.

Acknowledgments
This work was made possible by the financial support of Fondo CONACYT-SENER/Sustentabilidad Energética through the Centro Mexicano de Inovación en Energías del Océano (CEMIE-Océano), grant number 249795; and DPRI research funds, JSPS KAKENHI and Integrated Research Program for Advancing Climate Models (TOUGOU Program: JPMXD0717935498) supported by the MEXT of Japan. Special thanks to the STI Group of IIngen-UNAM for their continued support in computer equipment.

References

Alves, J. H. (2006). Numerical modeling of ocean swell contributions to the global wind-wave climate. *Ocean Modelling*, *11*, (1–2), 98–122. https://doi.org/10.1016/j.ocemod.2004.11.007

Ashok, K., Behera, S. K., Rao, S. A., Weng, H., & Yamagata, T. (2007). El Niño Modoki and its possible teleconnection. *Journal of Geophysical Research*, *112*, (C11), L03803. https://doi.org/10.1029/2006jc003798

Babanin, A. V., Rogers, W. E., de Camargo, R., Doble, M., Durrant, T., Filchuk, K., et al. (2019). Waves and Swells in high wind and extreme fetches, measurements in the Southern Ocean. *Frontiers in Marine Science*, *6*. https://doi.org/10.3389/fmars.2019.00361

Barnard, P. L., Hoover, D., Hubbard, D. M., Snyder, A., Ludka, B. C., Allan, J., et al. (2017). Extreme oceanographic forcing and coastal response due to the 2015–2016 El Niño. *Nature Communications*, *8*, 14365.

Barnard, P. L., Short, A. D., Harley, M. D., D Splinter, K., Vitousek, S., Turner, I. L., et al. (2015). Coastal vulnerability across the Pacific dominated by El Niño/southern oscillation. *Nature Geoscience*, *8*(10), 801–807.

Bromirski, P. D., Cayan, D. R., Helly, J., & Wittmann, P. (2013). Wave power variability and trends across the North Pacific. *Journal of Geophysical Research: Oceans*, *118*(12), 6329–6348. https://doi.org/10.1002/2013JC009189

Cai, W., Santoso, A., Wang, G., Yeh, S.W, An, S., Cobb, K. M., et al. (2015). ENSO and greenhouse warming. *Nature Climate Change*, *5*(9), 849–859.

Hersbach, H., Bell, B., Berrisford, P., Hirahara, S., Horányi, A., Muñoz-Sabater, J., et al. (2020). The ERA5 global reanalysis. *Quarterly Journal of the Royal Meteorological Society*, *146*, (730), 1999–2049. https://doi.org/10.1002/qj.3803

Escudero, M., Silva, R., Hesp, P. A., & Mendoza, E. (2019). Morphological evolution of the sandspit at Tortugueros Beach, Mexico. *Marine Geology*, *407*, 16–31.

Fogt, R. L., & Bromwich, D. H. (2006). Decadal variability of the ENSO teleconnection to the high-latitude South Pacific governed by coupling with the southern annular mode. *Journal of Climate*, *19*(6), 979–997.

Gavrikov, A. V., Krinitsky, M. A., & Grigorieva, V. G. (2016). Modification of Globwave satellite altimetry database for sea wave field diagnostics. *Oceanology*, *56*(2), 301–306.

Goodwin, I. D. (2005). A mid-shelf, mean wave direction climatology for southeastern Australia, and its relationship to the El Niño—Southern oscillation since 1878 A.D. *International Journal of Climatology*, *25*(13), 1715–1729.

Goodwin, I. D., Mortlock, T. R., & Browning, S. (2016). Tropical and extratropical-origin storm wave types and their influence on the east Australian longshore sand transport system under a changing climate. *Journal of Geophysical Research: Oceans*, *121*(7), 4833–4853. https://doi.org/10.1002/2016JC011769

Guenther, H., Hasselmann, S., & Janssen, P. A. E. M. (1992). *The WAM model cycle 4*. Hamburg, Germany.

Hirsch, R. M., Slack, J. R., & Smith, R. A. (1982). Techniques of trend analysis for monthly water quality data. *Water Resources Research*, *18*(1), 107–121.

Kaufman, L., & Rousseeuw, P. J. (1990). *Finding groups in data: An introduction to cluster Analysis*, Antwerp, Belgium: John Wiley.

Kelly, J. T., McSweeney, S., Shulmeister, J., & Gontz, A. M. (2019). Bimodal climate control of shoreline change influenced by interdecadal Pacific oscillation variability along the cooloola sand mass, Queensland, Australia. *Marine Geology*, *415*, 105971.

Kendall, M. G. (1948). *Rank correlation methods*. Oxford, England: Griffin.

10.1029/2020JC016464

Lucas, C., Timbal, B., & Nguyen, H. (2014). The expanding tropics: A critical assessment of the observational and modeling studies. *Wiley Interdisciplinary Reviews: Climate Change*, *5*(1), 89–112.

Lu, J., Chen, G., & Frierson, D. M. W. (2008). Response of the zonal mean atmospheric circulation to El Niño versus global warming. *Journal of Climate*, *21*(22), 5835–5851.

Lu, J., Deser, C., & Reichler, T. (2009). Cause of the widening of the tropical belt since 1958. *Geophysical Research Letters*, *36*(3), L03803. https://doi.org/10.1029/2008GL036076

MacQueen, J. (1967). Some methods for classification and analysis of multivariate observations. In L. M. Le Cam & J. Neyman (Eds.), *Proceedings of the Fifth Berkeley Symposium on Mathematical Statistics and Probability, Volume 1: Statistics, Fifth Berkeley Symposium on Mathematical Statistics and Probability* (pp. 281–297). Berkeley, CA: University of California Press.

Medellín, G., & Torres-Freyermuth, A. (2019). Morphodynamics along a micro-Tidal sea breeze dominated beach in the vicinity of coastal structures. *Marine Geology*, *417*, 106013.

Menéndez, M., Méndez, F. J., Losada, I. J., & Graham, N. E. (2008). Variability of extreme wave heights in the Northeast Pacific Ocean based on buoy measurements. *Geophysical Research Letters*, *35*(22), 1–6. https://doi.org/10.1029/2008GL035394

Mori, N., Kishimoto, R., & Shimura, T. (2018). Wave climate variability and related climate indices. *Coastal Engineering Proceedings*, *1*(36), 75.

Morim, J., Hemer, M., Wang, X. L., Cartwright, N., Trenham, C., Semedo, A., et al. (2019). Robustness and uncertainties in global multivariate wind-wave climate projections. *Nature Climate Change*, *9*(9), 711–718.

Moron, V., & Gouirand, I. (2003). Seasonal modulation of the El Niño–southern oscillation relationship with sea level pressure anomalies over the North Atlantic in October–march 1873–1996. *International Journal of Climatology*, *23*(2), 143–155.

Mortlock, T. R., & Goodwin, I. D. (2016). Impacts of enhanced central Pacific ENSO on wave climate and Headland-Bay Beach morphology. *Continental Shelf Research*, *120*, 14–25.

Neelin, J. D., Battisti, D. S., Hirst, A. C., Jin, F.-F., Wakata, Y., Yamagata, T., et al. (1998). ENSO theory. *Journal of Geophysical Research*, *103*(C7), 14261–14290.

Odériz, I., Silva, R., Mortlock, T. R., & Mendoza, E. (2020). Climate drivers of directional wave power on the Mexican coast. *Ocean Dynamics*, *70*(9), 1253–1265.

Ranasinghe, R. (2016). Assessing climate change impacts on open sandy coasts: A review. *Earth-Science Reviews*, *160*, 320–332.

Rasmusson, E. M., & Carpenter, T. H. (1982). Variations in tropical sea surface temperature and surface wind fields associated with the southern oscillation/El Niño. *Monthly Weather Review*, *110*(5), 354–384.

Reguero, B. G., Losada, I. J., & Méndez, F. J. (2015). A global wave power resource and its seasonal, interannual and long-term variability. *Applied Energy*, *148*, 366–380.

Reguero, B. G., Losada, I. J., & Méndez, F. J. (2019). A recent increase in global wave power as a consequence of oceanic warming. *Nature Communications*, *10*(1), 1–14.

Reichler, T. (2009). Climate change. In T. Letcher (Ed.) *Changes in the atmospheric circulation as indicator of climate change* (pp. 145–164). Amsterdam, the Netherlands: Elsevier.

Reiter, E. R. (1978). The interannual variability of the ocean-atmosphere system. *Journal of the Atmospheric Sciences*, *35*(3), 349–370.

Ribal, A., & Young, I. R. (2019). 33 Years of globally calibrated wave height and wind speed data based on altimeter observations. *Scientific Data*, *6*(1), 77.

Ruiz de Alegría-Arzaburu, A., & Vidal-Ruiz, J. A. (2018). Beach recovery capabilities after El Niño 2015–2016 at Ensenada Beach, Northern Baja California. *Ocean Dynamics*, *68*(6), 749–759.

Santoso, A., McGregor, S., Jin, F. F., Cai, W., England, M. H., An, S., et al; (2013). Late-twentieth-century emergence of the El Niño propagation asymmetry and future projections. *Nature*, *504*(7478), 126–130.

Semedo, A., Sušelj, K., Rutgersson, A., & Sterl, A. (2010). A global view on the wind sea and swell climate and variability from ERA-40. *Journal of Climate*, *24*(5), 1461–1479.

Shimura, T., Mori, N., & Mase, H. (2013). Ocean waves and teleconnection patterns in the Northern hemisphere. *Journal of Climate*, *26*(21), 8654–8670.

Silva, R., Lithgow, D., Esteves, L. S., Martínez, M. L., Moreno-Casasola, P., Martell, R., et al. (2017). Coastal risk mitigation by green infrastructure in Latin America. *Proceedings of the Institution of Civil Engineers: Maritime Engineering*. *170*(2), 39–54.

Stopa, J. E., & Cheung, K. F. (2014). Periodicity and patterns of ocean wind and wave climate. *Journal of Geophysical Research: Oceans*, *119*(8), 5563–5584. https://doi.org/10.1002/2013JC009729

Storlazzi, C. D., & Griggs, G. B. (1998). Influence of El Niño-southern oscillation (ENSO) events on the coastline of central California. *Journal of Coastal Research*, (26), 146–153. https://www.jstor.org/stable/25736131

Storlazzi, C. D., & Reid, J. A. (2010). The influence of El Niño-southern oscillation (ENSO) cycles on wave-driven sea-floor sediment mobility along the central California continental margin. *Continental Shelf Research*, *30*(14), 1582–1599.

Takahashi, K., Montecinos, A., Goubanova, K., & Dewitte, B. (2011). ENSO regimes: Reinterpreting the canonical and Modoki El Niño. *Geophysical Research Letters*, *38*(10), L10704. https://doi.org/10.1029/2011GL047364

Timmermann, A., An, S. I., Kug, J. S., Jin, F. F., Cai, W., Capotondi, A., et al. (2018). El Niño–southern oscillation complexity. *Nature*, *559*(7715), 535–545. https://doi.org/10.1038/s41586-018-0252-6

Timmermans, B. W., Gommenginger, C. P., Dodet, G., & Bidlot, J. R. (2020). Global wave height trends and variability from new multimission satellite altimeter products, reanalyses, and wave buoys. *Geophysical Research Letters*, *47*(9), e2019GL086880.

Toimil, A., Camus, P., Losada, I. J., Le Cozannet, G., Nicholls, R. J., Idier, D., et al. (2020). Climate change-driven coastal erosion modelling in temperate sandy beaches: Methods and uncertainty treatment. *Earth-Science Reviews*, *202*, 103110.

Tolman, H. (2009). User manual and system documentation of WAVEWATCH III version 3.14. *NOAA/NWS/NCEP Technical Note*, *276*.194

Trenberth, K. E., & Hoar, T. J. (1997). El Niño and climate change. *Geophysical Research Letters*, *24*(23), 3057–3060.

Wahl, T., & Plant, N. G. (2015). Changes in erosion and flooding risk due to long-term and cyclic oceanographic trends. *Geophysical Research Letters*, *42*(8), 2943–2950. https://doi.org/10.1002/2015GL063876

Wallace, J. M., & Gutzler, D. S. (1981). Teleconnections in the geopotential height field during the Northern Hemisphere winter. *Monthly Weather Review*, *109*(4), 784–812.

Wang, H., Kumar, A., Wang, W., & Xue, Y. (2012). Influence of ENSO on Pacific decadal variability: An analysis based on the NCEP climate forecast system. *Journal of Climate*, *25*(18), 6136–6151.

Wang, B., Wu, R., & Fu, X. (2000). Pacific–East Asian teleconnection: How does ENSO affect east Asian climate? *Journal of Climate*, *13*(9), 1517–1536.

Webb, A., & Fox-Kemper, B. (2011). Wave spectral moments and Stokes drift estimation. *Ocean Modelling*, *40*(3), 273–288.

10.1029/2020JC016464

Yates, M. L., Guza, R. T., & O'Reilly, W. C. (2009). Equilibrium shoreline response: Observations and modeling. *Journal of Geophysical Research*, *114*(C9), C09014. https://doi.org/10.1029/2009JC005359

Young, I. R., Zieger, S., & Babanin, A. V. (2011). Global trends in wind speed and wave height. *Science 332*(6028), 451–455.

Zhang, W., Jin, F. F., Stuecker, M. F., Wittenberg, A. T., Timmermann, A., Ren, H. L., et al. (2016). Unraveling El Niño's impact on the east Asian monsoon and Yangtze river summer flooding. *Geophysical Research Letters*, *43*(21), 11311–11375, 11382. https://doi.org/10.1002/2016GL071190